



Magnetic Fields and Fragmentation of Filaments in the Hub of California-X

Eun Jung Chung¹ , Chang Won Lee^{2,3} , Woojin Kwon^{4,5} , Mario Tafalla⁶ , Shinyoung Kim² , Archana Soam⁷ , and Jungyeon Cho¹

¹ Department of Astronomy and Space Science, Chungnam National University, Daejeon, Republic of Korea; rigelej@gmail.com

² Korea Astronomy and Space Science Institute, 776 Daedeokdae-ro, Yuseong-gu, Daejeon 34055, Republic of Korea

³ University of Science and Technology, Korea (UST), 217 Gajeong-ro, Yuseong-gu, Daejeon 34113, Republic of Korea

⁴ Department of Earth Science Education, Seoul National University, 1 Gwanak-ro, Gwanak-gu, Seoul 08826, Republic of Korea

⁵ SNU Astronomy Research Center, Seoul National University, 1 Gwanak-ro, Gwanak-gu, Seoul 08826, Republic of Korea

⁶ Observatorio Astronómico Nacional (IGN), Alfonso XII 3, E-28014 Madrid, Spain

⁷ Indian Institute of Astrophysics, II Block, Koramangala, Bengaluru 560034, India

Received 2023 February 22; revised 2023 April 26; accepted 2023 May 11; published 2023 July 5

Abstract

We present 850 μm polarization and C¹⁸O (3-2) molecular line observations toward the X-shaped nebula in the California molecular cloud using James Clerk Maxwell Telescope (JCMT)’s SCUBA-2/POL-2 and HARP instruments. The 850 μm emission shows that the observed region includes two elongated filamentary structures (Fil1 and Fil2) having chains of regularly spaced cores. We measured the mass per unit length of the filaments and found that Fil1 and Fil2 are thermally super- and subcritical, respectively, but both are subcritical if nonthermal turbulence is considered. The mean projected spacings ($\Delta\bar{S}$) of the cores in Fil1 and Fil2 are 0.13 and 0.16 pc, respectively. $\Delta\bar{S}$ is smaller than $4\times$ the filament width expected in the classical cylinder fragmentation model. The large-scale magnetic field orientations shown by Planck are perpendicular to the long axes of Fil1 and Fil2, while those in the filaments obtained from the high-resolution polarization data of JCMT are disturbed, but those in Fil1 tend to have longitudinal orientations. Using the modified Davis–Chandrasekhar–Fermi method, we estimated the magnetic field strengths (B_{pos}) of the filaments, which are 110 ± 80 and $90 \pm 60 \mu\text{G}$, respectively. We calculated the gravitational, kinematic, and magnetic energies of the filaments, and found that the fraction of magnetic energy is larger than 60% in both filaments. We propose that the dominant magnetic energy may lead the filament to be fragmented into aligned cores as suggested by Tang et al., and the shorter core spacing can be due to a projection effect via the inclined geometry of the filaments or due to nonnegligible longitudinal magnetic fields in the case of Fil1.

Unified Astronomy Thesaurus concepts: [Interstellar magnetic fields \(845\)](#); [Interstellar medium \(847\)](#); [Polarimetry \(1278\)](#); [Submillimeter astronomy \(1647\)](#); [Star forming regions \(1565\)](#)

1. Introduction

Hub–filament systems (HFSs) are the best laboratories to investigate the initial conditions for star formation. HFSs consist of a hub with a high column density ($>10^{22} \text{ cm}^{-2}$), a low axis ratio, and several filaments with relatively low column densities and high aspect ratios extend from the hub (Myers 2009). They are mostly associated with active low- to high-mass star clusters (Kumar et al. 2020), and easily found both in nearby star-forming molecular clouds and more distant infrared dark clouds. Hence, HFSs have been studied using multiwavelength observations to understand how they form and how stars are generated in them (e.g., Kumar et al. 2020; Bhadari et al. 2022; Hwang et al. 2022).

The crucial process to form stars in hubs and filaments is fragmentation. It is believed that early star formation begins with the fragmentation of filaments in hydrostatic equilibrium state into cores due to linear perturbations (e.g., Ostriker 1964). With the assumption of an isothermal, infinitely long cylindrical structure, fragmentation in a filament occurs via gravitational perturbations with a critical wavelengths of two times the filament’s diameter, and filaments may have cores with a regular spacing of four times the diameter of the

filament, which is the fastest growing mode (e.g., Inutsuka & Miyama 1992). However, observed core separations are generally not matched to the spacing expected by the classical cylinder model (e.g., Tafalla & Hacar 2015; Zhang et al. 2020), probably because of other factors which can affect the fragmentation process of filaments such as turbulence, accreting flows, and/or magnetic fields (e.g., Fiege & Pudritz 2000; Clarke et al. 2016; Hanawa et al. 2017).

The main drivers of star formation are gravity, turbulence, and magnetic fields, although their precise roles, particularly during the fragmentation process from filamentary molecular clouds into dense cores, are still unclear. Recently, it has been proposed that the relative significance of these three factors can determine the different evolutionary paths from clumps on the scale of 2 pc to cores on the scale of 0.6 pc (Tang et al. 2019). Specifically, Tang et al. (2019) has classified fragmentation types into “clustered,” “aligned,” and “no” fragmentation based on the distribution of cores within natal clouds, with each type appearing to be closely related to the dominance of turbulence, magnetic fields, and gravity, respectively. However, more observational data of various filamentary molecular clouds with different fragmentation types are needed to understand better the precise roles of gravity, turbulence, and magnetic fields in star formation.

L1478 in the California molecular cloud is known as a low-mass star-forming cloud at a distance of 470 pc (Zucker et al. 2019). It has a prominent HFS to which Imara et al. (2017)



Original content from this work may be used under the terms of the [Creative Commons Attribution 4.0 licence](#). Any further distribution of this work must maintain attribution to the author(s) and the title of the work, journal citation and DOI.

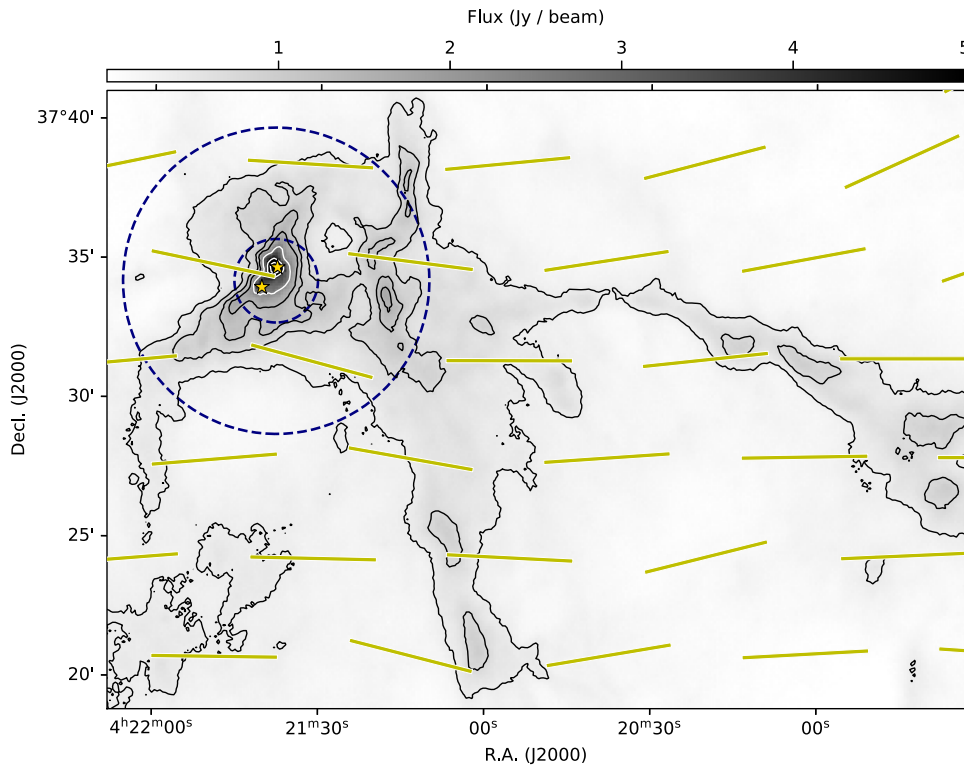


Figure 1. Herschel 250 μm image of the X-shaped nebula region in the California molecular cloud. The contour levels are 3, 6, 9, 12, 20, 40, and 70 σ ($1\sigma = 0.12 \text{ Jy beam}^{-1}$). The yellow segments depict the large-scale magnetic field orientations obtained by rotating the submillimeter Planck 353 GHz polarization orientations by 90°. The effective angular resolution is $\sim 5'$. The yellow stars denote YSOs found by Harvey et al. (2013). The JCMT SCUBA-2/POL-2 observing area of 11' diameter is indicated with the large dashed circle. The small dashed circle shows the inner 3' region with the best sensitivity.

refers to as California-X (shortly Cal-X) because of its X-shape. The Herschel 250 μm image of Cal-X given in Figure 1 shows that there are two long parsec-scale filaments radiating from the bright hub to the south and to the west, respectively. The mass of the hub is $\sim 130 M_{\odot}$ (Chung et al. 2019), and those of the filaments at the south and west are ~ 130 and $150 M_{\odot}$, respectively (Imara et al. 2017). The hub includes two young stellar objects (YSOs): one is Class I and the other is Class II (Harvey et al. 2013; Broekhoven-Fiene et al. 2014). The continuous velocity gradients of Cal-X indicate possible gas flow along the filaments into the hub (Imara et al. 2017; Chung et al. 2019). The Planck data show, though their resolution is limited ($\sim 5'$), that magnetic field orientations are mostly east-to-west, hence the long filament in the west is roughly parallel to the global B -field but the hub and the southern filament is perpendicular to the global B -field.

At the central 11' area of the hub, two elongated filamentary features can be seen. Zhang et al. (2020) investigated these filaments and dense cores in the hub of Cal-X. They showed that the cores are regularly spaced along the filaments where the core spacings are shorter than the expected spacing by the classical cylinder model (Inutsuka & Miyama 1992). We notice that the chain of cores in the filaments of the Cal-X hub is classified as aligned fragmentation, and thus the filaments are suitable to study the role of gravity, turbulence, and magnetic fields on the fragmentation of hub/filament into cores. We have performed high-resolution polarization observations and molecular line observations using the SCUBA-2/POL-2 and Heterodyne Array Receiver Programme (HARP) instruments mounted on the James Clerk Maxwell Telescope (JCMT) toward the hub of Cal-X. The paper is organized as follows. In Section 2, we describe the observations and data reduction. The

results of the observations and the measured magnetic field strength are depicted in Section 3. We present the analysis and discussion in Sections 4 and 5, respectively. A summary is given in Section 6.

2. Observations

2.1. Polarization Observations

We made submillimeter continuum and polarization observations at 850 μm toward the hub of the California-X molecular cloud. The observation was performed with the SCUBA-2/POL-2 instrument on the JCMT between 2019 October and 2021 January. The beam size at 850 μm wavelength is $14''.1$ (corresponding to $\sim 0.03 \text{ pc}$ at a distance of 470 pc). The standard SCUBA-2/POL-2 daisy mapping mode was used with a constant scanning speed of $8'' \text{ s}^{-1}$. The observations were done 21 times, with an average integration time of 40 minutes under dry weather conditions with submillimeter opacity at 225 GHz ($\tau_{225 \text{ GHz}}$) ranging between 0.05 and 0.08.

We used the `pol2map` script of the STARLINK/SMURF package for the 850 μm data reduction. The `pol2map` data reduction process consists of three steps. In the first step, the raw bolometer time streams for each observation are converted into separate Stokes I , Q , and U time streams using the process `calcqu`. In the second step, it produces improved I maps using a mask determined with the signal-to-noise ratio (S/N) via the process `makemap`. We set the parameter `SKYLOOP=TRUE` to reduce the dispersion between maps and lessen the intrinsic instabilities of the map-making algorithm.⁸ The final I map is

⁸ <http://starlink.eao.hawaii.edu/docs/sc22.htx/sc22.html>

created by coadding the improved individual I maps. In the final step, Q and U maps are produced from the Q and U time streams with the same masks used in the previous step. For the instrumental polarization correction, the “2019 August” IP model⁹ was used. The final I , Q , and U maps are binned with a pixel size of $4''$.

The polarized intensity (PI) is the quadratic sum of Q and U , $PI = \sqrt{Q^2 + U^2}$, and thus the noises of Q and U always make a positive contribution to the polarization intensity (e.g., Vaillancourt 2006). The debiased polarization intensity is estimated using the modified asymptotic estimator (Plaszczynski et al. 2014):

$$PI = \sqrt{Q^2 + U^2} - \sigma^2 \frac{1 - e^{-(Q^2+U^2)/\sigma^2}}{2\sqrt{Q^2 + U^2}}, \quad (1)$$

where σ^2 is the weighted mean of the variances on Q and U :

$$\sigma^2 = \frac{Q^2\sigma_Q^2 + U^2\sigma_U^2}{Q^2 + U^2}, \quad (2)$$

and σ_Q and σ_U are the standard errors in Q and U , respectively.

The debiased polarization fraction P is calculated as:

$$P = \frac{PI}{I}, \quad (3)$$

and its corresponding uncertainty is:

$$\sigma_P = \sqrt{\frac{\sigma^2}{I^2} + \frac{\sigma_I^2(Q^2 + U^2)}{I^4}}, \quad (4)$$

where σ_I is the standard error in I .

We used the final debiased polarization vector catalog provided with a bin size of $12''$ to increase the S/N of the polarization data. The $12''$ bin size is also close to the beam size of JCMT/POL-2 at $850 \mu\text{m}$, which is $14''.1$. The selection criteria of the polarization measurements are set to be (1) the S/N of the total intensity is larger than 10 ($I/\sigma_I > 10$) and (2) the polarization fraction is larger than two times its uncertainty ($P/\sigma_P > 2$).

A flux calibration factor (FCF) of $668 \text{ Jy pW}^{-1} \text{ beam}^{-1}$ is used for the $850 \mu\text{m}$ Stokes I , Q , and U data. This FCF is larger than the standard $850 \mu\text{m}$ SCUBA-2 flux conversion factor of $495 \text{ Jy pW}^{-1} \text{ beam}^{-1}$ because a correction factor of 1.35 is multiplied due to the additional losses from POL-2 (Dempsey et al. 2013; Friberg et al. 2016; Mairs et al. 2021). The rms noise values in the I , Q , and U binned to pixel size $12''$ are 3.2, 3.0, and $3.0 \text{ mJy beam}^{-1}$, respectively.

2.2. C^{18}O (3-2) Observations

We performed C^{18}O (3-2) line observations using HARP (Buckle et al. 2009) to estimate the velocity dispersion of the region. The data were taken as basket-weaved scan maps over three nights between 2020 January and 2022 July in weather band 2 ($\tau_{225 \text{ GHz}} \sim 0.065\text{--}0.08$). The spatial resolution is about $14''$, which is the same as that of the JCMT/POL-2 $850 \mu\text{m}$ data, and the spectral resolution is $\sim 0.05 \text{ km s}^{-1}$. The total observing time is ~ 6 hr. We reduced the data using the ORAC-DR pipeline in STARLINK software (Buckle et al. 2012) with a recipe of ‘REDUCE_SCIENCE_NARROWLINE’ and

obtained a data cube with a $14''$ pixel size. We resampled the data cube to a channel width of 0.1 km s^{-1} using a 1D Gaussian kernel. The mean rms level of the final data cube is about $0.06 \text{ K}[T_A^*]$.

3. Results

3.1. Identification of Filaments and Cores

The $850 \mu\text{m}$ Stokes I map is presented in Figure 2. The $850 \mu\text{m}$ emission closely matches the Herschel $250 \mu\text{m}$ emission of the hub presented in Figure 1. There are two elongated filamentary structures: one at the center and the other at the west.

We used the FILFINDER algorithm, which employs mathematical morphology to identify filaments (Koch & Rosolowsky 2015). FILFINDER takes five steps to identify filamentary structures. Simply introducing the algorithm here: it first flattens the image using an arctangent transform of $I' = I_0 \arctan(I/I_0)$ with the normalization of $I_0 \equiv \exp(\mu + 2\sigma)$, where μ and σ are the mean and standard deviation of the log-intensity. Second, it makes the flattened data to be smoothed with a Gaussian beam having an FWHM of 0.05 pc . And then, it creates a mask using an adaptive threshold of the smoothed data, i.e., it keeps pixels which have an intensity greater than the median value of the neighboring pixels within the distance of 0.1 pc , while discarding pixel having a lower intensity. In the fourth and fifth steps, small and spurious structures are removed, i.e., structures with sizes less than $5\pi(0.1 \text{ pc})^2$ are rejected, and small spurious features of the edges are also removed by applying a 0.05 pc size median filter.

Using FILFINDER, we obtained four filamentary structures as outlined with yellow in Figure 2. The filaments’ skeletons given by the algorithm are depicted with solid lines. The skeletons are found using a medial axis transform in which the chosen skeleton pixels are the centers of the inscribed circles of the mask. Then, the length of the filament is measured along the longest path through the skeleton after pruning the substructures. Among the identified four filaments, we make analyses for the two largest filaments, named filament 1 (Fil1) and filament 2 (Fil2), in this study.

The mass of filament is estimated with the following equation (e.g., Hildebrand 1983):

$$M = \frac{S_\nu d^2}{\kappa_\nu B_\nu(T_d)}, \quad (5)$$

where S_ν , κ_ν , and B_ν are the integrated flux density, opacity, and Planck function at the wavelength of $850 \mu\text{m}$, respectively. T_d and d are the dust temperature and the distance, respectively. The dust opacity is obtained by $\kappa_\nu = 0.1(\nu/10^{12} \text{ Hz})^\beta \text{ cm}^2 \text{ g}^{-1}$ with the assumption of a dust-to-gas ratio of 1:100 (Beckwith & Sargent 1991), and a dust opacity index of $\beta = 2$ (Draine & Lee 1984). The dust temperatures were taken from Herschel data (André et al. 2010; Chung et al. 2019). The applied T_d for Fil1 and Fil2 is $12.0 \pm 1.1 \text{ K}$ and $10.8 \pm 0.2 \text{ K}$, and then their masses were derived to be 15 ± 2 and $8 \pm 1 M_\odot$, respectively. The H_2 column density is calculated by dividing the mass in each pixel estimated from Equation (5) by the pixel area. The central H_2 column densities ($N_{\text{H}_2}^0$; the median value of N_{H_2} along the filament crest) are 13×10^{21} and $7 \times 10^{21} \text{ cm}^{-2}$ for Fil1 and Fil2, respectively. The filaments’ widths are estimated from a

⁹ <https://www.eoobservatory.org/jcmt/2019/08/new-ip-models-for-pol2-data/>

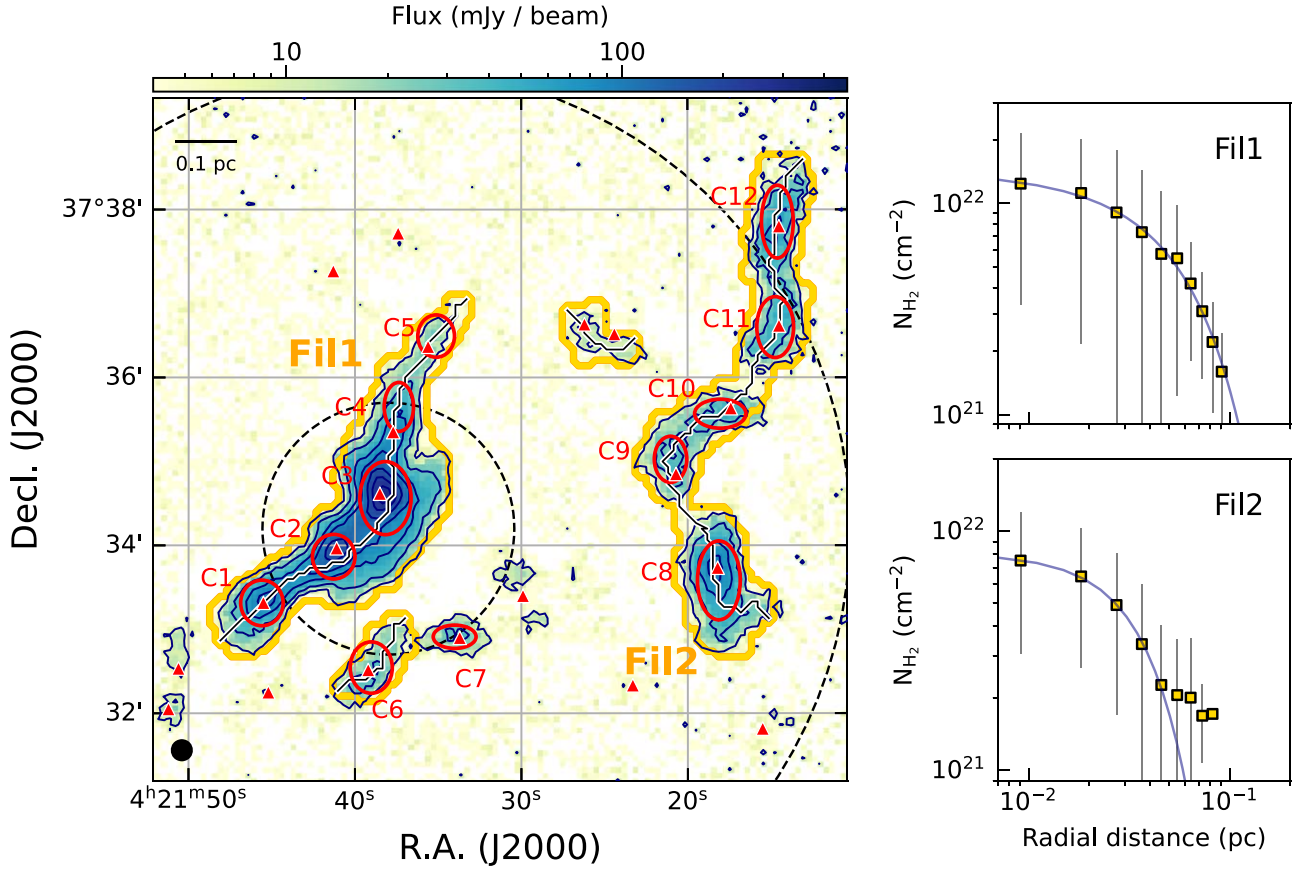


Figure 2. The observed 850 μm Stokes I image and contours. The contour levels are 3, 10, 20, 30, 50, 70, and 90 σ (1σ is 3.2 mJy beam $^{-1}$). Filaments identified with FILFINDER are presented with yellow polygons. The filaments' skeletons are drawn with solid lines. The red ellipses depict the 850 μm cores identified using FELLWALKER and the red triangles indicate the positions of cores identified with the Herschel data (Zhang et al. 2020). The dashed circles are the observing area of 11' diameter and the best sensitivity coverage of the 3' region. The black circle at the bottom left corner shows the POL-2 850 μm beam size of 14''. A reference scale of 0.1 pc is shown on the top left corner. Right: averaged radial column density profiles of filaments 1 and 2 centered on their skeletons (yellow squares) and their Gaussian fits to estimate the filaments' widths.

Table 1
Derived Physical Parameters of the Filaments

	Length (pc)	Width (pc)	$N_{\text{H}_2}^0$ (10^{21} cm^{-2})	\bar{n}_{H_2} (10^3 cm^{-3})	M (M_\odot)	M_{line} ($M_\odot \text{ pc}^{-1}$)	σ_{NT} (km s^{-1})
Fil1	0.73 ± 0.04	0.160 ± 0.026	13 ± 8	26 ± 16	15 ± 2	20 ± 3	0.41
Fil2	0.89 ± 0.05	0.070 ± 0.004	7 ± 5	33 ± 21	8 ± 1	9 ± 2	0.24

Note. M is the filament's mass estimated from Equation (5), $N_{\text{H}_2}^0$ is the median column density along the crest of the filament, \bar{n}_{H_2} is the average volume density given by $N_{\text{H}_2}^0/W$ by assuming that each filament is cylindrical, and M_{line} is the mass per unit length measured by dividing the mass by its length.

Gaussian fit to the averaged radial column density profiles shown in Figure 2. The mass per unit length (M_{line}) is estimated by dividing the mass by the length. M_{line} of Fil1 and Fil2 is 20 ± 3 and $9 \pm 2 M_\odot \text{ pc}^{-1}$, respectively. The physical properties of Fil1 and Fil2 are listed in Table 1.

Zhang et al. (2020) investigated Cal-X using a Herschel H_2 column density map. They used the *getfilaments* and *getsources* algorithms (Men'shchikov et al. 2012) to identify filaments and dense cores. Filaments #10 and #8 of Zhang et al. (2020) correspond to Fil1 and Fil2 of this study, respectively. Fil1 is longer and wider than F#10, but Fil2 is shorter and narrower than F#8. One noticeable thing is that the mass of F#8 is $26 M_\odot$ at the distance of 470 pc, which is about three times larger than Fil2. Besides, the measured line mass of

F#8 is $28 M_\odot \text{ pc}^{-1}$, implying that it is thermally supercritical while Fil2 is subcritical.

The differences can be caused by the different methods used for the identification of filaments, and the measurements used: the Herschel far-infrared data span from 70 to 500 μm wavelength and the JCMT submillimeter data were taken at 850 μm . In addition, we cannot rule out the possibility of underestimation due to the filtering out of structures with scales greater than a few arcminutes and/or decreasing sensitivity at radii larger than 3' of the POL-2 map obtained by the *daisy* scan mode (e.g., Holland et al. 2013). However, the $N_{\text{H}_2}^0$ values of Fil1 and Fil2 are consistent with those of F#10 ($12 \times 10^{21} \text{ cm}^{-2}$) and F#8 ($9.5 \times 10^{21} \text{ cm}^{-2}$). Besides, the average volume densities \bar{n}_{H_2} , the key physical quantity used to

calculate the magnetic field strength (B_{POS}) of Fil1 and Fil2, also agree to those of F#10 ($39 \times 10^3 \text{ cm}^{-3}$) and F#8 ($22 \times 10^3 \text{ cm}^{-3}$) within the uncertainties.

We used the FELLWALKER clump-finding algorithm (Berry 2015) to extract dense cores from the filaments. Pixels with intensities $>1\sigma$ are used to find cores, and an object having a peak intensity higher than 10σ and a size larger than $2 \times$ the beam size of $14''$ is identified as a real core. The FELLWALKER algorithm considers neighboring peaks are separated if the difference between the peak values and the minimum value (dip value) between the peaks is larger than the given threshold. We use 0.9σ as the threshold, and found five dense cores in each of the Fil1 and Fil2 regions, as shown in Figure 2. The dense cores identified from the Herschel H_2 column density map (Zhang et al. 2020) are presented with red triangles. The positions of $850 \mu\text{m}$ cores are consistent with those of Herschel dense cores. C4, C5, and C9 have offsets, but within one beam size of JCMT.

To estimate the velocity dispersions of the filaments, we used C^{18}O (3-2) data. Figure 3 shows the moment maps of C^{18}O (3-2) and the averaged spectra of Fil1 and Fil2. The moment 0 map is integrated over the velocity range between -2.5 and 0.8 km s^{-1} . The peak position of the integrated C^{18}O (3-2) emission is well matched to that of the $250 \mu\text{m}$ as well as of $850 \mu\text{m}$ emission. Fil2 has a relatively lower C^{18}O intensity than Fil1. The velocity field of the region can be seen in the moment 1 map. The central velocities of Fil1 and Fil2 are about -1.3 km s^{-1} and -0.2 km s^{-1} , respectively. Fil2 shows a relatively large velocity range between -1.0 to 0 km s^{-1} , while the velocity field of Fil1 gradually changes from -1.5 to -1.2 km s^{-1} only.

The averaged spectra of Fil1 and Fil2 are given in Figure 3. The averaged spectrum of Fil1 is fairly well fitted with a single Gaussian profile, but that of Fil2 seems to have two velocity components. To investigate the velocity field of Fil2 in detail, we inspected the spectra over the regions and presented the averaged spectra of dense cores in Fil2 in the figure. We performed single and double Gaussian fitting for the spectra and overlaid the resulting Gaussian profiles on the spectra. The spectra of C10, C11, and C12, which are placed in the northern part of Fil2, look like they have a single velocity component, but those of C8 and C9 at the south appear to have two velocity components. Moreover, the blue components of C8 and C9 are likely connected to the south of Fil2 (see the moment 1 map and spectrum of the ‘‘South of Fil2’’ core at the bottom right panel). Hence, we performed a multicomponent Gaussian fit to the averaged spectrum of Fil2 and selected the red component as a kinematic tracer of Fil2 between the two Gaussian components, with central velocities at -0.5 km s^{-1} and 0 km s^{-1} . This is reasonable because the red components of the cores’ spectra are well connected along the whole filament, while the blue components appear to start from the south and extend to the middle of Fil2. We notice that Fil2, which is identified using the $850 \mu\text{m}$ continuum data, may include substructures (so-called fibers) having different velocities at the south. However, it is beyond this paper’s scope to investigate magnetic fields. Therefore, we leave the identification and analysis of the fibers for our future study.

The nonthermal velocity dispersion (σ_{NT}) is calculated by extracting the thermal velocity dispersion (σ_{T}) from the observed total velocity dispersion (σ_{obs}):

$$\sigma_{\text{NT}} = \sqrt{\sigma_{\text{obs}}^2 - \sigma_{\text{T}}^2}. \quad (6)$$

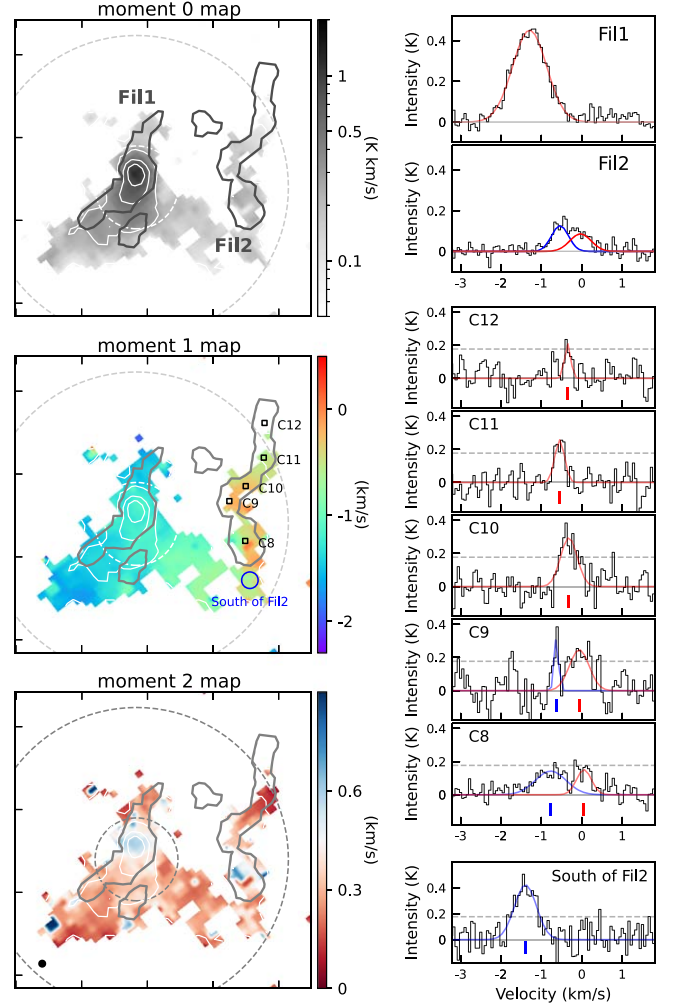


Figure 3. Left: C^{18}O (3-2) moment maps. The contours of the C^{18}O (3-2) integrated intensity are overlaid on the moment maps depicted with gray or color tones, and the contour levels are $3, 10, 20,$ and 30σ ($1\sigma = 0.03 \text{ K km s}^{-1}$). The outlines of filaments are drawn with solid polygons. The dashed circles present the POL-2 observation area of $11'$ diameter and its best sensitivity coverage of the $3'$ region. The open squares in the moment 1 map depict the positions of dense cores in Fil2. The black circle at the bottom left of the moment 2 map shows the FWHM beam size at the C^{18}O (3-2) frequency. Right: the averaged spectra of the filaments and dense cores. Red profiles overlaid on the spectra are the Gaussian fit results of the filaments and dense cores, and the blue profiles are the second Gaussian components. The spectrum shown in the bottom panel is the averaged one of the southern region of Fil2 depicted with the blue circle on the moment 1 map, i.e., printed as ‘‘South of Fil2.’’

The observed total velocity dispersion is taken from the Gaussian fit result as mentioned in the previous paragraph and shown in Figure 3. The thermal velocity dispersion of the observed molecules is:

$$\sigma_{\text{T}} = \sqrt{\frac{k_{\text{B}}T}{\mu_{\text{obs}}m_{\text{H}}}}, \quad (7)$$

where k_{B} , T , μ_{obs} , and m_{H} are the Boltzmann constant, gas temperature, atomic weight of the observed molecule (30 for C^{18}O), and the hydrogen mass, respectively. As for the gas temperature, we used the dust temperature obtained from the Herschel continuum data. The estimated nonthermal velocity dispersions are given in Table 1.

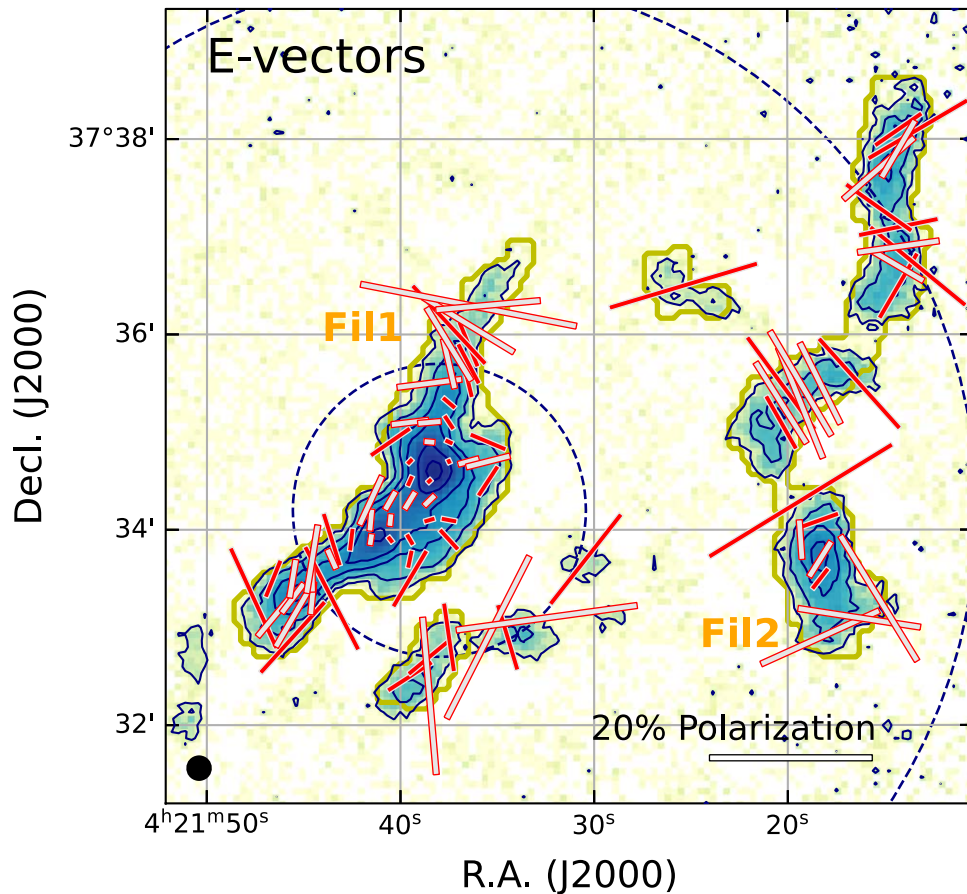


Figure 4. Polarization vectors on the $850\ \mu\text{m}$ emission. A reference scale of the polarization fraction (20%) is shown in the lower right corner of the figure. The red and white face colors denote the polarization vectors with $2 < P/\sigma_P \leq 3$ and $P/\sigma_P > 3$, respectively. The contour levels of $850\ \mu\text{m}$, the navy dashed circles, and the black circle in the lower left corner are the same as in Figure 2.

3.2. Polarization Properties

Dust polarization occurs because nonspherical dust grains tend to align their minor axes parallel to the local magnetic field. This alignment results in a measurable polarization angle that can be used to estimate the strength of the interstellar magnetic field. Additionally, the polarization fraction (P) of thermal dust has an important meaning as an indicator of the dust alignment efficiency. Though the observed polarization fraction is affected by the mixing of various strengths, the amount of disorder of magnetic fields along the line of sight, as well as dust opacity, it is still used to investigate the dust alignment efficiency. The power-law index α of $P \propto I^{-\alpha}$ is used as a parameter of dependence of P on I . $\alpha = 0$ means that the dust grains align with the same efficiency at all optical depths, and $\alpha = 0.5$ implies a linear decrement of grain alignment efficiency as the optical depth incremental increases. $\alpha = 1$ describes the case where the dust grains at higher densities do not align in any special direction, but exist only in a thin layer on the surface of the cloud where the dust grains align.

Figure 4 shows polarization vectors on the $850\ \mu\text{m}$ Stokes I map. The polarization segments with $I/\sigma_I > 10$ are presented, and those with $2 < P/\sigma_P \leq 3$ and $P/\sigma_P > 3$ are represented with red and white filled lines, respectively. It appears that the polarization fraction is lower in the brighter region. This anticorrelation of polarization fraction with intensity is more clearly presented in Figure 5. In the left panel, the debiased

polarization fraction (P_{db}) as a function of the normalized I intensity is shown, and a least-squares single power-law fit of $P_{db} = P_{\sigma_{QU}}(I/\sigma_{QU})^{-\alpha}$ is overlaid with gray lines. The power-law index α with vectors of $I/\sigma_I > 10$ is 0.75 ± 0.09 , and that with vectors of $I/\sigma_I > 10$ and $P/\sigma_P > 2$ is 0.89 ± 0.06 .

Pattle et al. (2019) reported that the single power-law model, which is only applicable to high S/N data with $\alpha < 0.3$, may overestimate both α and $P_{\sigma_{QU}}$ with increasing α , whereas the Ricean-mean model generally performs well around $\alpha \sim 0.7$. Hence, we applied the Ricean-mean model to the nonbiased data with $I/\sigma_I > 10$ with the following equation (Pattle et al. 2019):

$$P = \sqrt{\frac{\pi}{2}} \left(\frac{I}{\sigma_{QU}} \right)^{-1} \mathcal{L}_{\frac{1}{2}} \left[-\frac{P_{\sigma_{QU}}^2}{2} \left(\frac{I}{\sigma_{QU}} \right)^{2(1-\alpha)} \right], \quad (8)$$

where $\mathcal{L}_{\frac{1}{2}}$ is a Laguerre polynomial of order $\frac{1}{2}$. The relationship between the nonbiased P and I is presented in the right panel of Figure 5 with the best-fitting model. The obtained best Ricean-mean model parameters are $\alpha = 0.65 \pm 0.13$ and $P_{\sigma_{QU}} = 0.20 \pm 0.08$.

Molecular clouds are expected to have a value of α between 0.5 and 1, and those investigated by the BISTRO survey are reported to have α in a range of 0.8 and 1.0 with a single power-law model (Kwon et al. 2018; Soam et al. 2018; Coudé et al. 2019; Liu et al. 2019; Ngoc et al. 2021; Kwon et al. 2022). The reported α of the Ricean-mean model for the

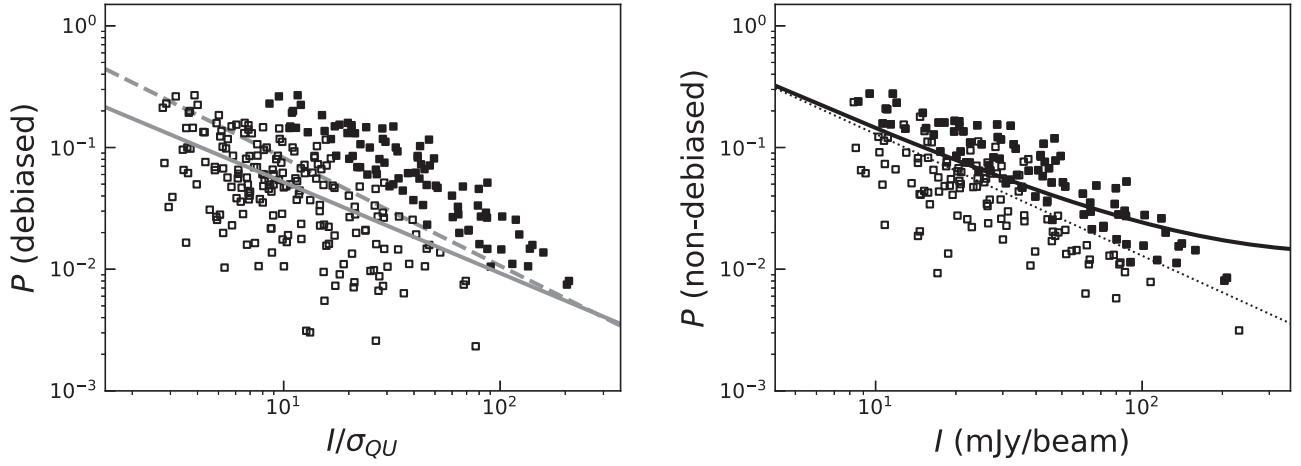


Figure 5. Polarization fraction as a function of Stokes I intensity. The selection criterion of $I/\sigma_I > 10$ is used, and the open and filled symbols indicate those with $P/\sigma_P \leq 2$ and $P/\sigma_P > 2$, respectively. Left: relationship between the debiased P and the normalized Stokes I intensity with $\sigma_{QU} = 3.0 \text{ mJy beam}^{-1}$ (the rms noise in both Stokes Q and U measurements). The solid gray line shows the best fit to a single power-law function between the debiased P and I/σ_{QU} . The obtained power-law slope α and $P_{\sigma_{QU}}$ are 0.75 ± 0.09 and 0.29 ± 0.05 , respectively. The dashed line shows vectors with $P/\sigma_P > 2$, and the obtained $\alpha = 0.89 \pm 0.06$ and $P_{\sigma_{QU}} = 0.63 \pm 0.06$. Right: dependence of the nondebiased P on I is presented. The solid black line is the best-fitting Ricean-mean model. The obtained power-law slope α and $P_{\sigma_{QU}}$ are 0.65 ± 0.13 and 0.20 ± 0.08 , respectively. The dotted black line indicates the null hypothesis case ($\alpha = 0$).

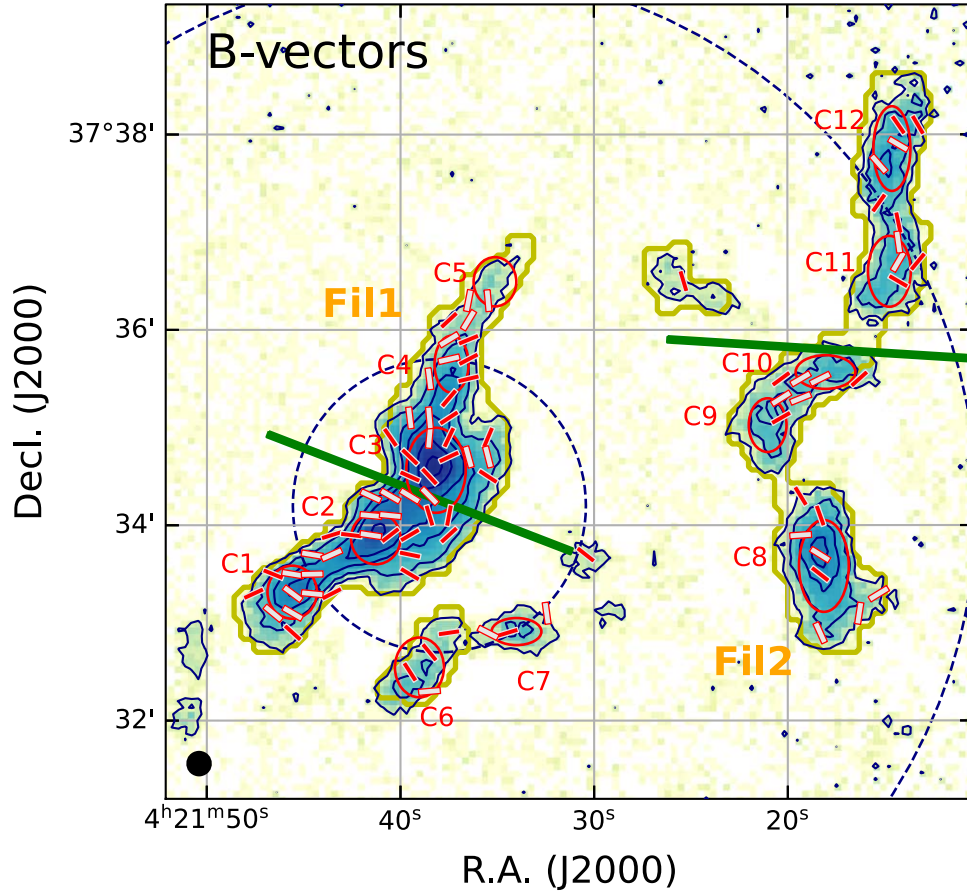


Figure 6. The magnetic field orientations. The lengths of the B -field segments are equally given to show the magnetic field orientation better. The red and white face colors denote the vectors with $2 < P/\sigma_P \leq 3$ and $P/\sigma_P > 3$, respectively. The green segments depict the large-scale B -field orientations of each filament deduced from the Planck 353 GHz polarization vectors. The contour levels of $850 \mu\text{m}$, the navy dashed circles, and the black circle in the lower left corner are the same as in Figure 2.

BISTRO targets are 0.34 (Ophiuchus A), 0.6–0.7 (Oph B and C regions), 0.56 (IC 5146), 0.36 (Orion A), 0.30–0.34 (DR21 filament), and 0.35 (Monoceros R2; e.g., Pattle et al. 2019; Wang et al. 2019; Lyo et al. 2021; Ching et al. 2022; Hwang et al. 2022). The power-law index α of Cal-X hub obtained

using the Ricean-mean model is steeper than those of the Gould Belt molecular clouds having $\alpha \sim 0.3$, but similar to those of Oph B and C regions. The power-law index α of ~ 0.65 indicates that grain alignment still occurs inside the cloud, but its efficiency decreases in the dense regions. This trend can be

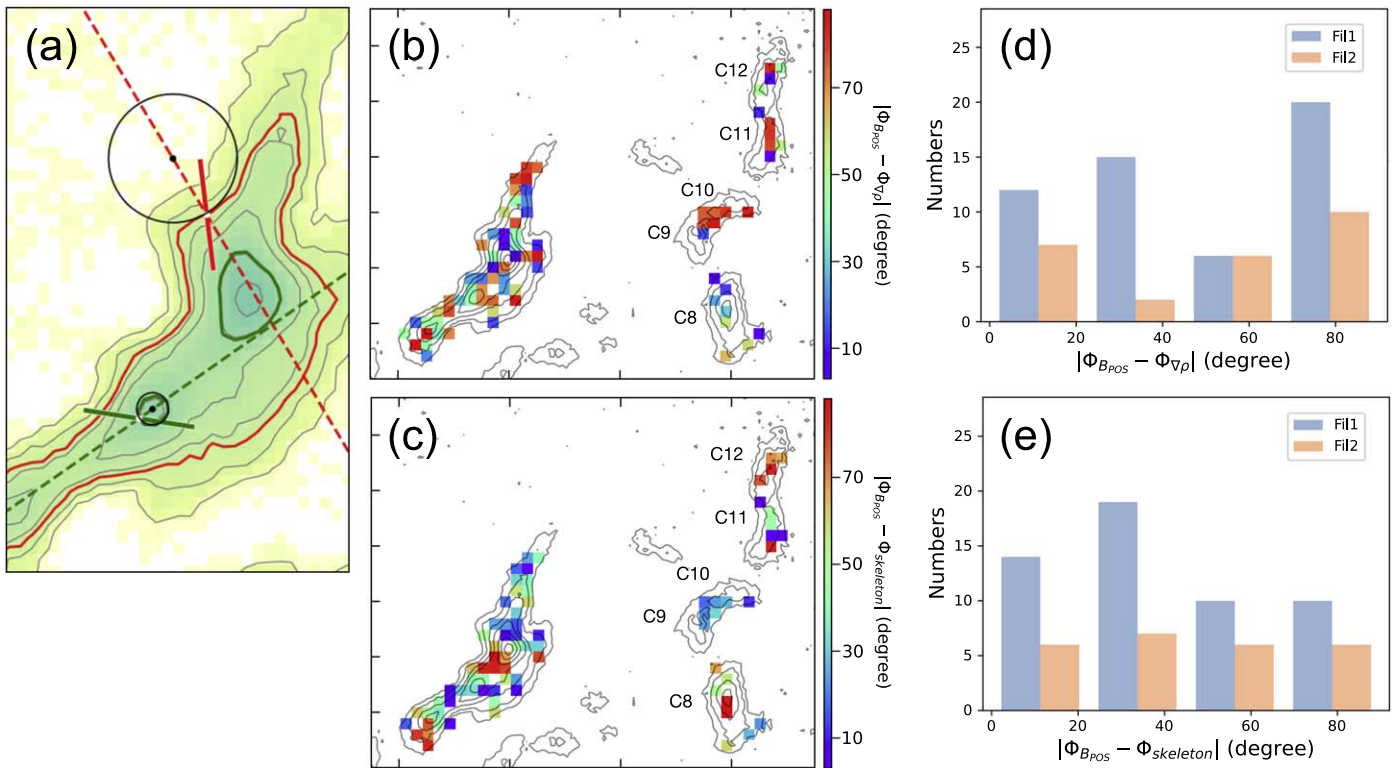


Figure 7. Example for the direction of density gradient measurement ((a), see the text), angle differences between the magnetic fields and the density gradient (b) and the skeleton (c), and their number distributions in histograms ((d) and (e)). An angle difference of zero (and 90°) means the parallel (and perpendicular) B -fields to the density gradient in panels (b) and (d) and to the skeleton in panels (c) and (e).

explained by the recent grain alignment theory where the decreasing radiation field and the increasing density and grain sizes at the dense regions lower the grain alignment efficiency (e.g., Hoang et al. 2021).

3.3. Magnetic Field Morphology and Strength

3.3.1. Magnetic Field Morphology

As mentioned in the previous section, the dust grains tend to align their shorter axes parallel to the magnetic field direction. Hence, the magnetic field can be inferred by rotating the thermal dust polarization orientations by 90° . Figure 6 shows the magnetic field orientations in the region. They appear to be perpendicular to the contours (i.e., parallel to the density gradient) in some regions and parallel to the filament's skeleton in some other regions.

To investigate the relation of the B -field orientation to the density gradient and the direction of the filaments in more detail, we estimated the angle difference of the magnetic field ($\phi_{B_{POS}}$) with the density gradient ($\phi_{\nabla\rho}$) and with the direction of the filaments' skeletons ($\phi_{skeleton}$). The direction of the density gradient was determined from the least-squares circle of the contour line that corresponds to the density level. Figure 7(a) shows example $\phi_{\nabla\rho}$ measurements. First, a contour line is drawn for the intensity level of the magnetic field vector (red and green contours for the red and green B -field vectors, respectively). Then, a least-squares circle is obtained by applying the `SciPy.optimize.Least_squares_circle`¹⁰ code to contour points within a distance of 0.05 pc

(presented with solid circles). Finally, the direction of the center of the obtained circle is determined to be the direction of the density gradient at that point and green dashed lines for the red and green B -field vectors, respectively). The direction of each filament's skeleton is the tangent vector at each skeleton's position. For the B -field segment which is not on the skeleton, the nearest skeleton's position angle is applied to measure its angle difference.

The result is given in Figure 7. The 0° and 90° of $|\phi_{B_{POS}} - \phi_{\nabla\rho}|$ mean the parallel and perpendicular B -fields to the density gradient, respectively, and those of $|\phi_{B_{POS}} - \phi_{skeleton}|$ have the same and perpendicular B -fields to the skeleton's direction. For Fil1, we cannot find any special distribution of $|\phi_{B_{POS}} - \phi_{\nabla\rho}|$ as shown in the left panel of Figure 7. Meanwhile, the B -fields vectors in Fil1 are perpendicular to the skeleton in the center and the southeastern edge, while tend to be parallel to the skeleton in the other regions (see the middle panel of Figure 7). These distributions can be seen from the histograms given in the right panels in the figure. In the histogram of $|\phi_{B_{POS}} - \phi_{\nabla\rho}|$, the numbers of $|\phi_{B_{POS}} - \phi_{\nabla\rho}| < 45^\circ$ and $> 45^\circ$ are 27 and 26, respectively. However, in the relation of $\phi_{B_{POS}}$ and $\phi_{skeleton}$, the number of $|\phi_{B_{POS}} - \phi_{skeleton}| < 45^\circ$ is 33 and that of $> 45^\circ$ is 20. Hence, the longitudinal B -field segments are slightly more prominent in Fil1. The number of magnetic field vectors of Fil2 is small (25) compared to that of Fil1 (53). Near C9, C10, and C11, the magnetic fields look perpendicular to the density gradient but parallel to the direction of skeleton. The histograms show that the number of $|\phi_{B_{POS}} - \phi_{\nabla\rho}| < 45^\circ$ is 9 and $> 45^\circ$ is 16, and the numbers of $|\phi_{B_{POS}} - \phi_{skeleton}| < 45^\circ$ and $> 45^\circ$ are 13 and 12, respectively. Hence, the B -fields in Fil2 tend to be

¹⁰ https://scipy-cookbook.readthedocs.io/items/Least_Squares_Circle.html

perpendicular to the density gradient, but they do not have any relation with the direction of the skeleton.

3.3.2. Magnetic Field Strength

The strength of the magnetic field in the molecular clouds can be estimated using the equations for the angular dispersion of the magnetic field vectors, velocity dispersion, and number density of the gas obtained by assuming that the underlying magnetic field is uniform but distorted by turbulence. We used the modified Davis–Chandrasekhar–Fermi method (Davis 1951; Chandrasekhar & Fermi 1953) provided by Crutcher et al. (2004):

$$B_{\text{pos}} = Q_c \sqrt{4\pi\bar{\rho}} \frac{\sigma}{\delta\phi} \\ \approx 9.3 \sqrt{\bar{n}_{\text{H}_2}} \frac{\Delta v}{\delta\phi}, \quad (9)$$

where Q_c is the correction factor for the underestimation of the angular dispersion in the polarization map due to the beam integration effect and hence overestimation of the magnetic field strength, adopted as 0.5 from Ostriker et al. (2001). \bar{n}_{H_2} is the mean volume density of the molecular hydrogen in cm^{-3} , $\Delta v = \sigma_{\text{NT}} \sqrt{8 \ln 2}$ in km s^{-1} , and $\delta\phi$ is the magnetic field angular dispersion.

The mean H_2 volume density of $\bar{n}_{\text{H}_2} = N_{\text{H}_2}^0/W$ is used by assuming the filament to have a cylindrical shape and its diameter to be the measured filament’s width. Δv is measured from the nonthermal velocity dispersion given in Table 1.

The angular dispersion of the magnetic field orientations is measured using two different methods. The first one is the unsharp-masking method (Pattle et al. 2017) and the second one is the structure function (Hildebrand et al. 2009). The large-scale magnetic fields present in the Planck data appear to be uniform and oriented perpendicular to the filament’s long axis. However, magnetic fields inside the filaments are generally much more complex due to the interaction between turbulence, gravity, and stellar feedback. Several observational studies report the possible modification of magnetic fields by gravitational contraction, outflows and their shocks, stellar feedback of expanding ionization fronts of H II regions, and gas flows driven by gravity (e.g., Hull & Girart 2017; Pattle et al. 2017; Pillai et al. 2020; Arzoumanian et al. 2021; Eswariah et al. 2021; Kwon et al. 2022). The magnetic fields in the filaments of the Cal-X hub are also possibly modified by gravity and outflows associated with the two YSOs at the center (Imara et al. 2017). Hence, we applied the unsharp-masking method to measure the angular dispersion of the magnetic field distorted by turbulence motion by removing the underlying magnetic field geometry (Pattle et al. 2017). We smoothed the magnetic field map using a 3×3 pixel boxcar filter and then subtracted the smoothed map from the observed map. Then, we measured the angular dispersion from the residual map. The smoothed and residual values were calculated only when the number of data points in the 3×3 boxcar filter was at least three. Figure 8 shows a position angle map of the observed magnetic field vectors (left), smoothed position angle map (middle), and the residual map (right). The obtained angular dispersions are $\delta\phi = 11^\circ.8 \pm 2^\circ.6$ and $16^\circ.6 \pm 1^\circ.9$ for Fil1 and Fil2, respectively.

The unsharp-masking method is widely used to estimate angular dispersions in filaments and cores. However, it assumes

that the underlying B -field is approximately uniform within the boxcar filter, and thus it requires a well-sampled polarization map having a sufficient amount of polarization detected within the boxcar filter to yield a reliable underlying B -field morphology. If we choose polarization vectors having more than four neighboring polarization angles in their 3×3 pixel boxcar filter, the available number of polarization vectors decreases from 54 to 34 for Fil1 and from 24 to 4 for Fil2. The resulting $\delta\phi$ of Fil1 and Fil2 are $11^\circ.3$ and $2^\circ.9$, respectively. In this case, Fil1 has similar $\delta\phi$ with that obtained from the residual values having more than two neighboring pixels in the filter. However, Fil2 has a quite smaller $\delta\phi$ than that from the residual values having more than two neighboring pixels and it may not be reliable due to the limited number of samples. Hence, we applied another statistical analysis method, the structure function of polarization angles (Hildebrand et al. 2009).

Simply introducing the structure function method, the structure function of the angle difference in a map can be expressed as the following equation:

$$\langle \Delta\Phi^2(l) \rangle \equiv \frac{1}{N(l)} \sum_{i=1}^{N(l)} [\Phi(x) - \Phi(x+l)]^2, \quad (10)$$

where $\Phi(x)$ is the angle at position x , $\Delta\Phi(l) \equiv \Phi(x) - \Phi(x+l)$ is the angle difference between vectors with separation l , and $N(l)$ is the number of pairs of the vectors. The magnetic field is assumed to be composed of a large-scale magnetic field and a turbulent component. The contribution of the large-scale magnetic field to the dispersion function would be expected to increase almost linearly as l increases in the range $0 \leq l \ll d$ with the large-scale structured magnetic field scale d . The effect of turbulence on magnetic fields is expected to be (1) almost 0 as $l \rightarrow 0$, (2) its maximum at $l \sim$ the turbulent scale (δ), and (3) constant at $l > \delta$. Then, the Equation (10) can be written as:

$$\langle \Delta\Phi^2(l) \rangle_{\text{tot}} \simeq b^2 + m^2 l^2 + \sigma_{\text{M}}^2(l), \quad (11)$$

where b is the constant turbulent contribution to the magnetic angular dispersion at $\delta < l < d$. m characterizes the linearly increasing contribution of the large-scale magnetic field. $\sigma_{\text{M}}^2(l)$ is the correction term for the contribution of the measurement uncertainty when dealing with real data.

Figure 9 shows the corrected angular dispersion ($\langle \Delta\Phi^2(l) \rangle_{\text{tot}} - \sigma_{\text{M}}^2(l)$) as a function of distance l . We divided the data into distance bins with separations in the pixel size of $12''$, and operated best fits using the first three data points to fulfill the condition of $l \ll d$. b^2 is obtained from least-squares fitting the relation, and the estimated b of Fil1 and Fil2 is 19.3 and 15.8, respectively. The corresponding angular dispersion $\delta\phi = \sqrt{b^2/2}$ to be applied to the modified Davis–Chandrasekhar–Fermi method is $13^\circ.7 \pm 9^\circ.3$ and $11^\circ.2 \pm 7^\circ.8$ for Fil1 and Fil2, respectively.

The applied \bar{n}_{H_2} , Δv , $\delta\phi$, and measured magnetic field strengths are listed in Table 2. The magnetic field strengths of Fil1 and Fil2 using $\delta\phi$ from the unsharp-masking method are estimated to be 120 ± 40 and $60 \pm 20 \mu\text{G}$ and using $\delta\phi$ from the structure function method are 110 ± 80 and $90 \pm 60 \mu\text{G}$, respectively. B_{POS} estimated from the two methods agrees with each other within the uncertainties. Hereafter, we will use “UM” and “SF” to indicate whether the quantities are derived

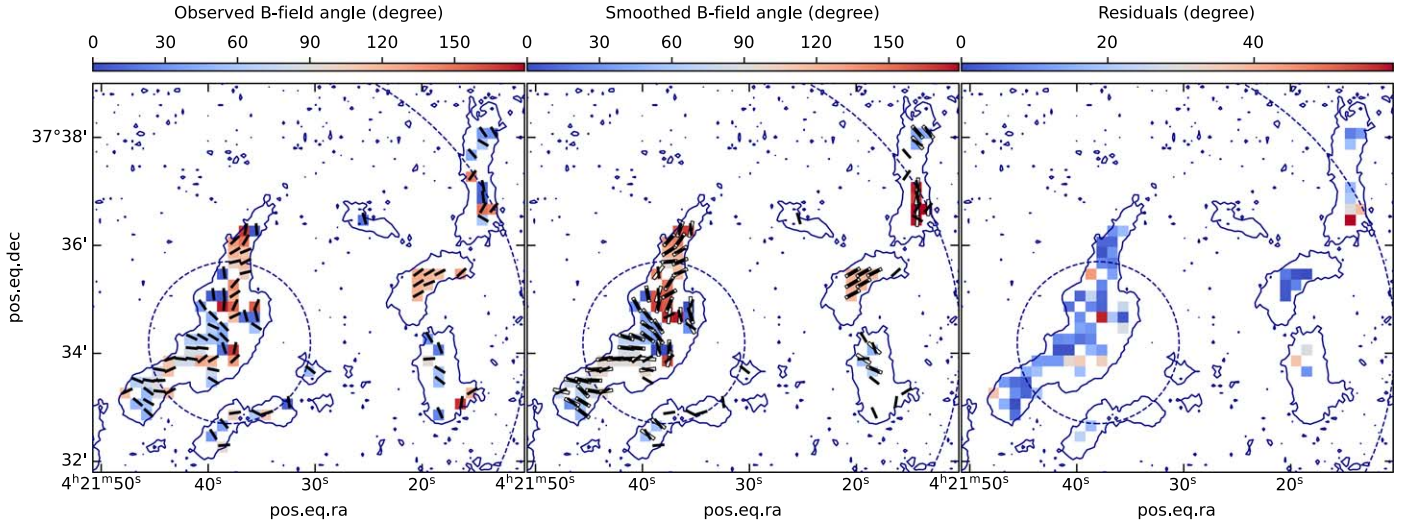


Figure 8. Position angle maps of magnetic field vectors observed (left) and smoothed with a 3×3 pixel boxcar filter (middle), and the residual map from subtracting the smoothed map from the observations (right). The observed B -field vectors (black line segment in the left and the middle panels) and the smoothed B -field vectors (white line segment in the middle panel) are presented in the images. The smoothed and residual values obtained when the number of polarization vectors in the 3×3 boxcar filter was less than three were excluded.

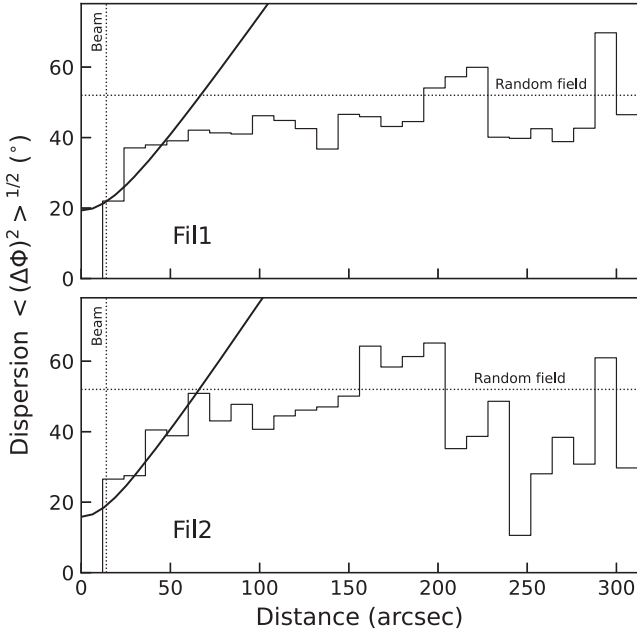


Figure 9. The angular dispersion function ($\langle (\Delta\Phi)^2 \rangle^{1/2}$) for Fil1 (top) and Fil2 (bottom). The best-fit model is presented with the thick solid curve, and the zero intercept of the fit determines the turbulent contribution to the total angular dispersion. The vertical and horizontal dotted lines indicate the beam size of POL-2 at the $850 \mu\text{m}$ wavelength ($14''$) and the expected $\langle (\Delta\Phi)^2 \rangle^{1/2}$ for a random field (52°), respectively.

using $\delta\phi$ from the unsharp-masking or structure function methods, respectively.

4. Analysis

4.1. Magnetic Field Strength, Gravity, and Turbulence

The main drivers of star formation in the interstellar medium are the gravity, turbulence, and magnetic fields. To investigate the significance of magnetic fields, we estimated the mass-to-magnetic flux ratio (λ) and Alfvénic Mach number (M_A).

The observed mass-to-magnetic flux ratio, $(M/\Phi)_{\text{obs}}$, is:

$$(M/\Phi)_{\text{obs}} = \frac{\mu_{\text{H}_2} m_{\text{H}} \bar{N}_{\text{H}_2}}{B_{\text{pos}}}, \quad (12)$$

where μ_{H_2} is the mean molecular weight per hydrogen molecule of 2.8, and \bar{N}_{H_2} is the median value of the central H_2 column density. The observed mass-to-magnetic flux ratio is compared with the critical mass-to-magnetic flux ratio of:

$$(M/\Phi)_{\text{crit}} = \frac{1}{2\pi\sqrt{G}}, \quad (13)$$

and the mass-to-magnetic flux ratio (λ_{obs}) is:

$$\lambda_{\text{obs}} = \frac{(M/\Phi)_{\text{obs}}}{(M/\Phi)_{\text{crit}}}. \quad (14)$$

Following Crutcher et al. (2004), we can write Equation (14) as:

$$\lambda_{\text{obs}} = 7.6 \times 10^{-21} \bar{N}_{\text{H}_2} / B_{\text{pos}}, \quad (15)$$

with \bar{N}_{H_2} in cm^{-2} and B_{pos} in μG . The real λ is assumed to be $\lambda_{\text{obs}}/3$ using a statistical correction factor of 3 for the random inclination of the filament (Crutcher et al. 2004). It is expected that magnetic fields support the clouds if λ is less than 1, while the structure would gravitationally collapse if λ is greater than 1. Fil1 and Fil2 have λ^{UM} of 0.27 ± 0.11 and 0.31 ± 0.10 and λ^{SF} of 0.31 ± 0.24 and 0.21 ± 0.16 , respectively, and hence they are likely supported by magnetic fields.

The Alfvénic Mach number (M_A) is estimated by:

$$M_A = \frac{\sigma_{\text{NT}}}{V_A}, \quad (16)$$

where σ_{NT} is the nonthermal velocity dispersion and V_A is the Alfvén velocity, which is defined as:

$$V_A = \frac{B}{\sqrt{4\pi\rho}}, \quad (17)$$

Table 2
B-Field Strengths of the Filaments

	Fil1		Fil2	
\bar{n}_{H_2} (10^3 cm^{-3})	26.4 ± 3.5		32.7 ± 4.7	
Δv (km s^{-1})	1.0 ± 0.3		0.6 ± 0.2	
$\delta\phi$ (degree)	UM	SF	UM	SF
	11.8 ± 2.6	13.7 ± 9.3	16.6 ± 1.9	11.2 ± 7.8
B_{pos} (μG)	120 ± 40	110 ± 80	60 ± 20	90 ± 60
λ	0.27 ± 0.11	0.31 ± 0.24	0.31 ± 0.10	0.21 ± 0.16
V_A (km s^{-1})	1.25 ± 0.44	1.08 ± 0.80	0.53 ± 0.16	0.79 ± 0.59
M_A	0.33 ± 0.15	0.38 ± 0.30	0.46 ± 0.18	0.31 ± 0.24
E_B ($M_\odot \text{ km}^2 \text{ s}^{-2}$)	11.4 ± 4.3	8.5 ± 6.4	1.2 ± 0.4	2.6 ± 2.0
E_G ($M_\odot \text{ km}^2 \text{ s}^{-2}$)	1.3 ± 0.3		0.3 ± 0.1	
E_K ($M_\odot \text{ km}^2 \text{ s}^{-2}$)	3.0 ± 1.5		0.8 ± 0.4	

where B is the total magnetic field strength and $\bar{\rho}$ is the mean density. The statistical average value of B_{pos} , $(4/\pi)B_{\text{pos}}$, is used for B (Crutcher et al. 2004), and the mean density is obtained from $\mu_{\text{H}_2} m_{\text{H}} \bar{n}_{\text{H}_2}$. Fil1 and Fil2 have V_A^{UM} of 1.25 ± 0.44 and $0.53 \pm 0.16 \text{ km s}^{-1}$ and V_A^{SF} of 1.08 ± 0.80 and $0.79 \pm 0.59 \text{ km s}^{-1}$, respectively. The Alfvénic Mach numbers of the two filaments are in the range 0.3–0.5, and hence Fil1 and Fil2 are sub-Alfvénic, indicating magnetic fields dominate the turbulence in these regions.

4.2. Energy Balance

We calculated the total gravitational, kinematic, and magnetic field energies in Fil1 and Fil2. The gravitational energy is calculated from the equation:

$$E_G^{\text{cylinder}} = -\frac{GM^2}{L}, \quad (18)$$

where M and L are the mass and length of the filament, respectively (Fiege & Pudritz 2000). The total kinematic energy is derived as:

$$E_K^{\text{cylinder}} = M\sigma_{\text{tot}}^2, \quad (19)$$

where σ_{tot} is the observed total velocity dispersion (e.g., Fiege & Pudritz 2000) estimated with the mean free particle of molecular weight $\mu_p = 2.37$ (Kauffmann et al. 2008) by the equation:

$$\sigma_{\text{tot}} = \sqrt{\sigma_{\text{NT}}^2 + \frac{k_B T}{\mu_p m_{\text{H}}}}. \quad (20)$$

The magnetic energy is calculated with the equation:

$$E_B = \frac{1}{2} M V_A^2. \quad (21)$$

The estimated values of the gravitational, kinematic, and magnetic energies in the filaments are tabulated in Table 2. Fil1 has larger E_G , E_K , and E_B by a factor of ~ 4 than Fil2, and this is likely related to the larger mass and nonthermal velocity dispersion of Fil1 than in Fil2. However, interestingly, the relative portions of energies are found to be similar in both filaments. The relative portions of energies are presented by donut diagrams in Figure 10. E_B^{SF} is used for the energy

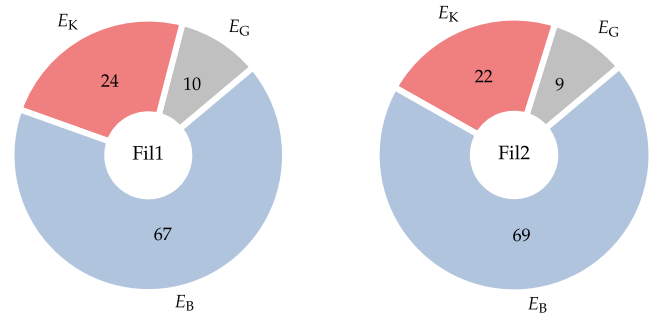


Figure 10. The relative portions of gravitational energy (E_G), kinematic energy (E_K), and magnetic energy (E_B^{SF}) of Fil1 (left) and Fil2 (right). E_G , E_K , and E_B^{SF} are presented with gray, red, and blue colors, respectively, and the relative portions are given in percent.

portions. As shown in the figure, both Fil1 and Fil2 have the largest portion of energy as magnetic energy ($>60\%$), and the smallest portion as gravitational energy ($\sim 10\%$). If E_B^{UM} is used, the energy portion of E_B^{UM} is 73% and 51% for Fil1 and Fil2, respectively, and the magnetic energy is still dominant in both filaments.

5. Discussion

The filaments in the hub of Cal-X have chains of dense cores with quasiperiodic spacings which can be the results of fragmentation due to gravitational instabilities. In the filaments' regime, the mass per unit length ($M_{\text{line}} = M/L$) of a filament is often used as a probe of a filament's instability, like the Jeans mass for spherical systems. In the hydrostatic isothermal cylinder model, the critical line mass ($M_{\text{line}}^{\text{th.crit}}$) where the thermal pressure is in equilibrium with gravitational collapse is calculated by the equation:

$$M_{\text{line}}^{\text{th.crit}} = \frac{2c_s^2}{G}, \quad (22)$$

where c_s is the sound speed. $M_{\text{line}}^{\text{th.crit}}$ is close to $16 M_\odot \text{ pc}^{-1}$ at the typical gas temperature of 10 K. The line masses of Fil1 and Fil2 are 20 ± 3 and $9 \pm 2 M_\odot \text{ pc}^{-1}$, respectively, and hence Fil1 is thermally supercritical and Fil2 is subcritical. If nonthermal components in the turbulence, which can also support the system from gravitational collapse, are considered,

the critical line mass including both nonthermal and thermal components ($M_{\text{line}}^{\text{crit}}$) can be calculated using the total velocity dispersion (σ_{tot}) instead of c_s with the following equation:

$$M_{\text{line}}^{\text{crit}} = \frac{2\sigma_{\text{tot}}^2}{G}. \quad (23)$$

$M_{\text{line}}^{\text{crit}}$ of Fil1 and Fil2 is ~ 96 and $45 M_{\odot} \text{pc}^{-1}$, respectively, and both filaments can be subcritical.

The two filaments in the hub of Cal-X are in a subcritical state if turbulence and thermal support are considered. However, they have the apparent fragmentation features of the chains of dense cores. This seems to contradict the major paradigm for core formation where dense cores form in gravitationally supercritical filaments via fragmentation. However, fragmentation and core formation in thermally subcritical and transcritical filaments are reported in several molecular clouds in observations (see Pineda et al. 2022, and references therein). This is also supported by a recent simulation study. Chira et al. (2018) show that when dynamic compression from the surrounding cloud is considered, filaments start to fragment when they are still subcritical. Alternatively, we note that the line mass estimated from the total mass and length (M/L) is the average value, and thus the filaments can be partly supercritical especially in dense regions. We estimated the local line mass (m_{line}) from the H_2 column density along the crest by multiplying the filament width ($N_{\text{H}_2} \times W$), as shown in Figure 11. The scale of the line mass is presented on the right y-axis. More than two core regions in each filament appear to be thermally supercritical ($>16 M_{\odot} \text{pc}^{-1}$), and the central core (C3) in Fil1 has a line mass larger than $M_{\text{line}}^{\text{crit}}$.

We also note that filaments could be either stabilized or destabilized by the geometry of the magnetic field: a magnetic field perpendicular to the filament's major axis has no contribution in supporting the filaments against radial collapse, while a magnetic field oriented parallel to the filament's major axis stabilizes the filament against radial contraction (e.g., Seifried & Walch 2015). In Figure 11, the central core (C3) region is locally supercritical ($m_{\text{line}} > M_{\text{line}}^{\text{crit}}$), and the magnetic field orientations in the region are perpendicular to the filament's long axis (see Figures 6 and 7(c)). This may indicate that the perpendicular B -field at the center can allow the radial accretion of the surrounding gas material onto the filament and the filament can be locally supercritical.

Tang et al. (2019) have argued that the energy balance of gravity, turbulence, and magnetic fields affect the fragmentation features of filamentary molecular clouds. According to their arguments, filamentary molecular clouds which are dominant in E_B would have aligned fragmentation, while those dominant in E_G and in E_K would have no and clustered fragmentations, respectively. Chung et al. (2022) investigated the relative importance of energy in a filament and hubs of HFSs in IC 5146, and obtained results which partly supported Tang et al. (2019)'s suggestion. Chung et al. (2022) proposed that E_G -dominant hubs are divided into the clustered and no fragmentation types according to their portion of kinematic energy.

The hub region of California-X shows elongated filamentary structures in $850 \mu\text{m}$, named Fil1 and Fil2 in this study, and the filaments have aligned fragmentation features. Their energy proportions clearly show that magnetic energy is dominant in both filaments. The fraction of E_B^{SF} in Fil1 and Fil2 is 67% and 69%, respectively, which agree with Tang et al. (2019)'s

suggestion. Moreover, the relative fractions of E_G , E_K , and E_B as well as the proportion of E_B in Fil1 and Fil2 are comparable to those of the filament in IC 5146 (Chung et al. 2022).

One more noticeable characteristics in the aligned fragmentation of Fil1 and Fil2 is the quasiperiodic spacing of cores. In our $850 \mu\text{m}$ data, five cores are identified in each filament. Figure 11 depicts the $850 \mu\text{m}$ intensity along the skeletons of filaments and the cores' positions. The mean projected spacings of the cores in Fil1 and Fil2 are 0.13 ± 0.01 and 0.16 ± 0.03 pc, respectively.

In the classical linear fragmentation models (e.g., Inutsuka & Miyama 1992), the core spacing is expected to be $\sim 4 \times$ the filament's width for infinitely long cylindrical filaments in hydrostatic equilibrium states. The width of Fil1 is 0.160 ± 0.026 pc and that of Fil2 is 0.070 ± 0.004 pc. The core spacings are much smaller than the expected value in the classical scenario. Since we do not correct for inclination, the mean projected spacings of the cores are lower limits. If the inclination to the line of sight is 12° and 35° for Fil1 and Fil2, respectively, the core spacings of Fil1 and Fil2 become 0.64 pc and 0.28 pc, coming close to four times each filament's width. However, the quasiperiodic spacings of fragments in filaments in observations (e.g., Smith et al. 2023) and simulations (e.g., Clarke et al. 2016) do not always match the expectations of classical cylinder model.

Zhang et al. (2020) used Herschel far-infrared data and investigated the filaments and cores in the California-X region. Four and five cores are found in Fil1 and Fil2 (filaments #10 and #8 in Zhang et al. 2020), respectively, and the cores are regularly spaced with $\Delta \bar{S}$ of 0.12 and 0.16 pc, respectively, assuming a distance of 470 pc. These are similar to our results from $850 \mu\text{m}$ data. The widths of the filaments estimated using Herschel data are 0.09 pc for Fil1 and 0.13 pc for Fil2 (Zhang et al. 2020), and thus $\Delta \bar{S}$ is smaller than the expected core spacing in the classical cylinder fragmentation model. They propose two possibilities for the short core spacings: (1) the geometrical bending structure of the filaments and (2) the continuous accretion of gas from the natal cloud in the case of F#8 (Fil2 in this study).

The role of magnetic fields on the fragmentation of filaments in Cal-X is also discussed by Zhang et al. (2020). The fragmentation intervals become shorter as the longitudinal magnetic fields become stronger (Nakamura et al. 1993). On the contrary, the magnetic fields perpendicular to the filament axis are proposed to increase the fragmentation intervals (Hanawa et al. 2017). Zhang et al. (2020) suggested that longitudinal magnetic fields with $\sim 100 \mu\text{G}$ can cause the short core spacings in the filaments of the Cal-X hub. The $B_{\text{POS}}^{\text{SF}}$ of Fil1 and Fil2 is 110 ± 80 and $90 \pm 60 \mu\text{G}$, respectively, which are comparable to the suggestion of Zhang et al. (2020). Beside, in the case of Fil1, the longitudinal magnetic fields are likely more prominent than the perpendicular magnetic fields (see Section 3.3). There are magnetic field orientations perpendicular to the filament's direction, but those vectors are confined to the central and southern regions with a portion of 38% only. And, they are strongly linked to the direction of the density gradient and the large-scale B -field orientation observed by Planck. Hence, we propose that the short core spacing of Fil1 in the Cal-X hub could be due to the longitudinal magnetic field orientation.

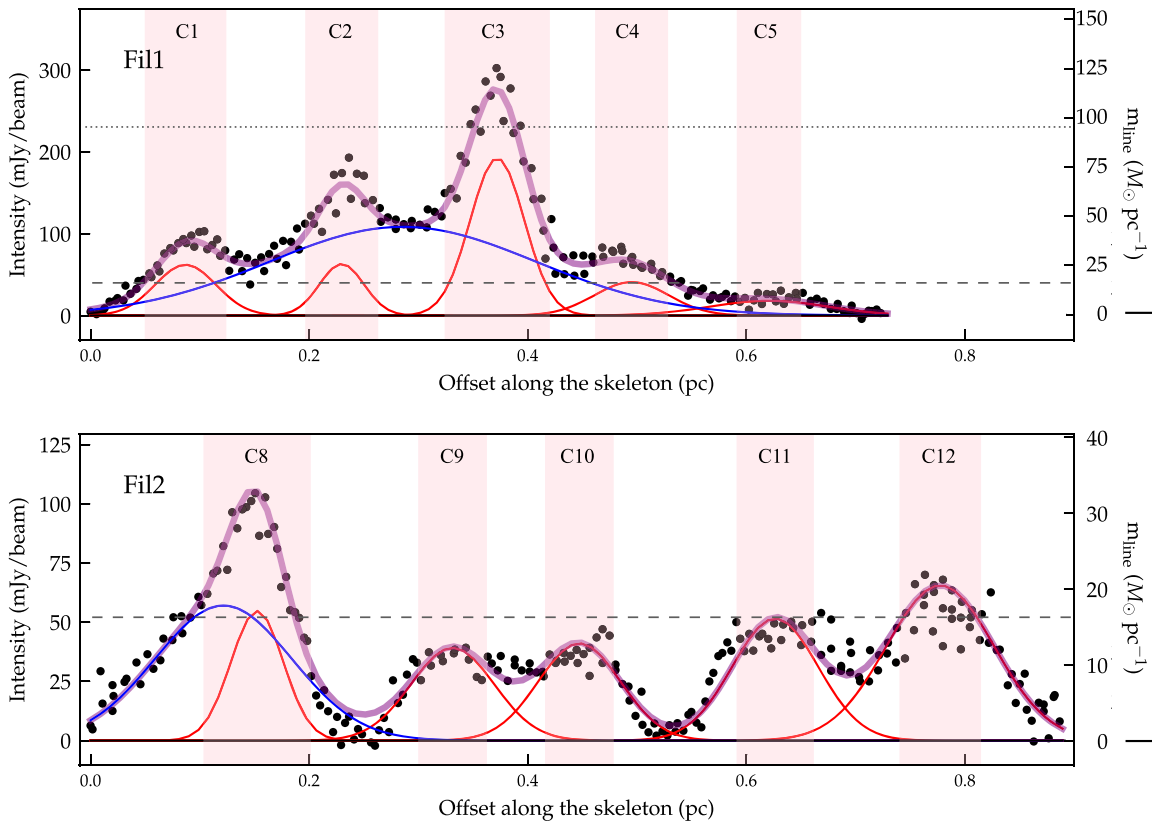


Figure 11. $850\ \mu\text{m}$ intensity (left y-axis) and its corresponding local line mass (m_{line} , right y-axis) along the skeleton from south to north. Pixels having distances <0.1 pc from the skeletons are used. The red and blue curves are the Gaussian models for the dense cores and background filament, respectively, and the thick purple curve is their sum. The pink colored regions indicate the positions and mean sizes of the dense cores. The dashed gray lines indicate $M_{\text{line}}^{\text{th,crit}}$ at the typical gas temperature of 10 K ($16 M_{\odot} \text{pc}^{-1}$), and the dotted line in the top panel is the $M_{\text{line}}^{\text{crit}}$ of Fil1 ($96 M_{\odot} \text{pc}^{-1}$).

6. Summary

We have performed polarization and molecular line observations toward the hub of the California-X molecular cloud using JCMT’s SCUBA-2/POL-2 and HARP instruments. The main results are summarized below.

1. We identified filaments and cores from the $850\ \mu\text{m}$ emission, and estimated physical quantities such as length, width, mass, and nonthermal velocity dispersions for two filaments (Fil1 and Fil2), which have chains of dense cores. The average line mass (M/L) shows that Fil1 and Fil2 are thermally supercritical and subcritical, respectively, but both are highly subcritical if nonthermal turbulence is considered.
2. The magnetic field vectors are inferred by rotating the polarization vectors by 90° . We measured the magnetic field strengths of the two filaments using the modified Davis–Chandrasekhar–Fermi method, which are $B_{\text{POS}}^{\text{SF}} = 110 \pm 80$ and $90 \pm 60\ \mu\text{G}$, respectively. The mass-to-magnetic flux ratios (λ) and Alfvénic Mach numbers (M_A) are calculated, and the two filaments are both magnetically subcritical and sub-Alfvénic.
3. We estimated the gravitational, kinematic, and magnetic field energies in the two filaments and compared the energy budgets. We found that magnetic energy has the largest fraction, of 67% and 69% in Fil1 and Fil2, respectively. Both filaments in the hub of Cal-X have cores in a line, which may be the result of filament fragmentation. The fragmentation types of the two

filaments can be classified into aligned fragmentation and the resulting energy balance is consistent with Tang et al. (2019)’s suggestion.





4. The mean projected core spacing of Fil1 and Fil2 is 0.13 and 0.16 pc, respectively, and they are smaller than that expected by the classical cylinder fragmentation model ($\sim 4\times$ the filament width). An inclination of 11° and 35° to the line of sight can explain the difference between the observed projected core spacing and the model’s core separation of Fil1 and Fil2, respectively. Besides, longitudinal magnetic fields are found to be slightly dominant in Fil1. Hence, we propose that the dominant, longitudinal B -fields may affect the fragmentation of Fil1 into aligned dense cores with a short core spacing.

Acknowledgments

The authors are grateful to the anonymous referee for the valuable comments, which helped to improve the quality of the paper. This research was supported by Basic Science Research Program through the National Research Foundation of Korea (NRF) funded by the Ministry of Education (grant No. NRF-2022R1I1A1A01053862) and the National R & D Program through the National Research Foundation of Korea Grants funded by the Korean Government (NRF-2016R1D1A1B02015014). C. W.L. was supported by the Basic Science Research Program through the National Research Foundation of Korea (NRF) funded by the Ministry of Education, Science and Technology (NRF-2019R1A2C1010851), and by the Korea Astronomy and Space

Science Institute grant funded by the Korea government (MSIT; project No. 2022-1-840-05). W.K. was supported by the National Research Foundation of Korea (NRF) grant funded by the Korea government (MSIT) (NRF-2021R1F1A1061794). M.T. acknowledges partial support from project PID2019-108765GB-I00 funded by MCIN/AEI/10.13039/501100011033. S.K. is supported by the National Research Council of Science & Technology (NST)-Korea Astronomy and Space Science Institute (KASI) Postdoctoral Research Fellowship for Young Scientists at KASI in South Korea.

ORCID iDs

Eun Jung Chung  <https://orcid.org/0000-0003-0014-1527>
 Chang Won Lee  <https://orcid.org/0000-0002-3179-6334>
 Woojin Kwon  <https://orcid.org/0000-0003-4022-4132>
 Mario Tafalla  <https://orcid.org/0000-0002-2569-1253>
 Shinyoung Kim  <https://orcid.org/0000-0001-9333-5608>
 Archana Soam  <https://orcid.org/0000-0002-6386-2906>
 Jungyeon Cho  <https://orcid.org/0000-0003-1725-4376>

References

- André, P., Men'shchikov, A., Bontemps, S., et al. 2010, *A&A*, **518**, L102
 Arzoumanian, D., Furuya, R. S., Hasegawa, T., et al. 2021, *A&A*, **647**, A78
 Beckwith, S. V. W., & Sargent, A. I. 1991, *ApJ*, **381**, 250
 Berry, D. S. 2015, *A&C*, **10**, 22
 Bhadari, N. K., Dewangan, L. K., Ojha, D. K., Pirogov, L. E., & Maity, A. K. 2022, *ApJ*, **930**, 169
 Broekhoven-Fiene, H., Matthews, B. C., Harvey, P. M., et al. 2014, *ApJ*, **786**, 37
 Buckle, J. V., Davis, C. J., Francesco, J. D., et al. 2012, *MNRAS*, **422**, 521
 Buckle, J. V., Hills, R. E., Smith, H., et al. 2009, *MNRAS*, **399**, 1026
 Chandrasekhar, S., & Fermi, E. 1953, *ApJ*, **118**, 113
 Ching, T.-C., Qiu, K., Li, D., et al. 2022, *ApJ*, **941**, 122
 Chira, R. A., Kainulainen, J., Ibáñez-Mejía, J. C., Henning, T., & Mac Low, M. M. 2018, *AJ*, **610**, A62
 Chung, E. J., Lee, C. W., Kim, S., et al. 2019, *ApJ*, **877**, 114
 Chung, E. J., Lee, C. W., Kwon, W., et al. 2022, *AJ*, **164**, 175
 Clarke, S. D., Whitworth, A. P., & Hubber, D. A. 2016, *MNRAS*, **458**, 319
 Coudé, S., Bastien, P., Houde, M., et al. 2019, *ApJ*, **877**, 88
 Crutcher, R. M., Nutter, D. J., Ward-Thompson, D., & Kirk, J. M. 2004, *ApJ*, **600**, 279
 Davis, L. 1951, *PhRv*, **81**, 890
 Dempsey, J. T., Friberg, P., Jenness, T., et al. 2013, *MNRAS*, **430**, 2534
 Draine, B. T., & Lee, H. M. 1984, *ApJ*, **285**, 89
 Eswaraiah, C., Li, D., Furuya, R. S., et al. 2021, *ApJL*, **912**, L27
 Fiege, J. D., & Pudritz, R. E. 2000, *MNRAS*, **311**, 85
 Friberg, P., Bastien, P., Berry, D., et al. 2016, *Proc. SPIE*, **9914**, 991403
 Hanawa, T., Kudoh, T., & Tomisaka, K. 2017, *ApJ*, **848**, 2
 Harvey, P. M., Fallscheer, C., Ginsburg, A., et al. 2013, *ApJ*, **764**, 133
 Hildebrand, R. H. 1983, *QJRAS*, **24**, 267
 Hildebrand, R. H., Kirby, L., Dotson, J. L., Houde, M., & Vaillancourt, J. E. 2009, *ApJ*, **696**, 567
 Hoang, T., Tram, L. N., Lee, H., Diep, P. N., & Ngoc, N. B. 2021, *ApJ*, **908**, 218
 Holland, W. S., Bintley, D., Chapin, E. L., et al. 2013, *MNRAS*, **430**, 2513
 Hull, C. L. H., Girart, J. M., Tychoniec, Ł., et al. 2017, *ApJ*, **847**, 92
 Hwang, J., Kim, J., Pattle, K., et al. 2022, *ApJ*, **941**, 51
 Imara, N., Lada, C., Lewis, J., et al. 2017, *ApJ*, **840**, 119
 Inutsuka, S.-i., & Miyama, S. M. 1992, *ApJ*, **388**, 392
 Kauffmann, J., Bertoldi, F., Bourke, T. L., Evans, N. J. I., & Lee, C. W. 2008, *AJ*, **487**, 993
 Koch, E. W., & Rosolowsky, E. W. 2015, *MNRAS*, **452**, 3435
 Kumar, M. S. N., Palmeirim, P., Arzoumanian, D., & Inutsuka, S. I. 2020, *A&A*, **642**, A87
 Kwon, J., Doi, Y., Tamura, M., et al. 2018, *ApJ*, **859**, 4
 Kwon, W., Pattle, K., Sadavoy, S., et al. 2022, *ApJ*, **926**, 163
 Liu, J., Qiu, K., Berry, D., et al. 2019, *ApJ*, **877**, 43
 Lyo, A. R., Kim, J., Sadavoy, S., et al. 2021, *ApJ*, **918**, 85
 Mairs, S., Dempsey, J. T., Bell, G. S., et al. 2021, *AJ*, **162**, 191
 Men'shchikov, A., André, P., Didelon, P., et al. 2012, *A&A*, **542**, A81
 Myers, P. C. 2009, *ApJ*, **700**, 1609
 Nakamura, F., Hanawa, T., & Nakano, T. 1993, *PASJ*, **45**, 551
 Ngoc, N. B., Diep, P. N., Parsons, H., et al. 2021, *ApJ*, **908**, 10
 Ostriker, E. C., Stone, J. M., & Gammie, C. F. 2001, *ApJ*, **546**, 980
 Ostriker, J. 1964, *ApJ*, **140**, 1056
 Pattle, K., Lai, S.-P., Hasegawa, T., et al. 2019, *ApJ*, **880**, 27
 Pattle, K., Ward-Thompson, D., Berry, D., et al. 2017, *ApJ*, **846**, 122
 Pillai, T. G. S., Clemens, D. P., Reissl, S., et al. 2020, *NatAs*, **4**, 1195
 Pineda, J. E., Arzoumanian, D., André, P., et al. 2022, arXiv:2205.03935
 Płaszczynski, S., Montier, L., Levrier, F., & Tristram, M. 2014, *MNRAS*, **439**, 4048
 Seifried, D., & Walch, S. 2015, *MNRAS*, **452**, 2410
 Smith, S. E. T., Friesen, R., Marchal, A., et al. 2023, *MNRAS*, **519**, 285
 Soam, A., Pattle, K., Ward-Thompson, D., et al. 2018, *ApJ*, **861**, 65
 Tafalla, M., & Hacar, A. 2015, *A&A*, **574**, A104
 Tang, Y.-W., Koch, P. M., Peretto, N., et al. 2019, *ApJ*, **878**, 10
 Vaillancourt, J. E. 2006, *PASP*, **118**, 1340
 Wang, J.-W., Lai, S.-P., Eswaraiah, C., et al. 2019, *ApJ*, **876**, 42
 Zhang, G.-Y., André, P., Men'shchikov, A., & Wang, K. 2020, *A&A*, **642**, A76
 Zucker, C., Speagle, J. S., Schlafly, E. F., et al. 2019, *ApJ*, **879**, 125